The Astronomical Journal, 130:1–12, 2005 July

THE NEAR-INFRARED CAMERA AND MULTI-OBJECT SPECTROMETER ULTRA DEEP FIELD: OBSERVATIONS, DATA REDUCTION, AND GALAXY PHOTOMETRY

Rodger I. Thompson
Steward Observatory, University of Arizona, 933 North Cherry Avenue, Tucson, AZ 85721

Garth Illingworth and Rychard Bouwens
Astronomy Department, University of California, Santa Cruz, CA 95064

Mark Dickinson
National Optical Astronomy Observatory, Tucson, AZ 85719

Daniel Eisenstein and Xiaohui Fan
Steward Observatory, University of Arizona, 933 North Cherry Avenue, Tucson, AZ 85721

Marijn Franx
Leiden Observatory, Postbus 9513, 2300 RA Leiden, Netherlands

Adam Riess
Space Telescope Science Institute, Baltimore, MD 21218

Marcia J. Rieke, Glenn Schneider, and Elizabeth Stobie
Steward Observatory, University of Arizona, 933 North Cherry Avenue, Tucson, AZ 85721

and

Sune Toft and Pieter van Dokkum
Department of Astronomy, Yale University, New Haven, CT 06520
Received 2004 December 14; accepted 2005 March 22

ABSTRACT

This paper describes the observations and data reduction techniques for the version 2.0 images and catalog of the Near-Infrared Camera and Multi-Object Spectrometer Ultra Deep Field (NICMOS UDF) Treasury program. All sources discussed in this paper are based on detections in the combined NICMOS F110W and F160W bands only. The NICMOS images are drizzled to $0\farcs09$ pixel^{-1} and aligned to the Advanced Camera for Surveys UDF F850LP image, which was rebinned to the same pixel scale. These form the NICMOS version 2.0 UDF images. The catalog sources are chosen with a conservative detection limit to avoid the inclusion of numerous spurious sources. The catalog contains 1293 objects in the $144'' \times 144''$ NICMOS subfield of the UDF. The 5 σ signal-to-noise ratio level is an average $0\farcs6$ diameter aperture AB magnitude of 27.7 at 1.1 and 1.6 μm. The catalog sources, listed in order of right ascension, satisfy a minimum signal-to-noise ratio criterion of 1.4 σ in at least seven contiguous pixels of the combined F110W and F160W image.

Key words: cosmology: observations — galaxies: fundamental parameters — galaxies: photometry

Online material: machine-readable table

1. INTRODUCTION

The Near-Infrared Camera and Multi-Object Spectrometer Ultra Deep Field (NICMOS UDF) Treasury observations were designed to complement and enhance the Advanced Camera for Surveys (ACS) optical UDF observations. They provide an extension in wavelength to 1.6 μm and two additional bands that extend the rest-band energy and morphology measurements to longer wavelengths. They also provide the potential for viewing objects at redshifts beyond 7.5, where Lyman lines and continuum absorption quench the flux in the ACS bands. The additional wavelength coverage also helps distinguish between the influences of age, metallicity, and extinction. As with previous deep-field catalog publications (Williams et al. 1996; Thompson et al. 1999; S. V. W. Beckwith 2005, in preparation), this paper is intended primarily as a description of the observations, data analysis, and source photometric properties rather than a scientific evaluation of the implications of the observations.

Due to the relatively small field of the NICMOS camera 3 used in this program ($51'' \times 51''$), only a subsection ($144'' \times 144''$) of the optical UDF was covered. This was done with a 3×3 tiling of the NICMOS images. The NICMOS images extend a few arcseconds beyond this subsection but at a significantly decreased signal-to-noise ratio. All the individual processed NICMOS images are available in the *Hubble Space Telescope* (*HST*) Treasury archive (MAST),[1] as are the raw images in the main *HST* archive.

The primary purpose of this paper is to provide a very detailed account of the data reduction steps used to produce the Treasury images and catalog stored in MAST so that users are aware of the pedigree of the data and can reproduce the analysis if they wish. Other users may wish to alter the reduction steps if they prefer choices other than the ones made here. Finally, we wish to convey the attributes and limitations of the catalog of sources. In particular, users who wish to extract the faintest sources from the data will want to use more aggressive

[1] See http://archive.stsci.edu/prepds/udf/udf_hlsp.html.

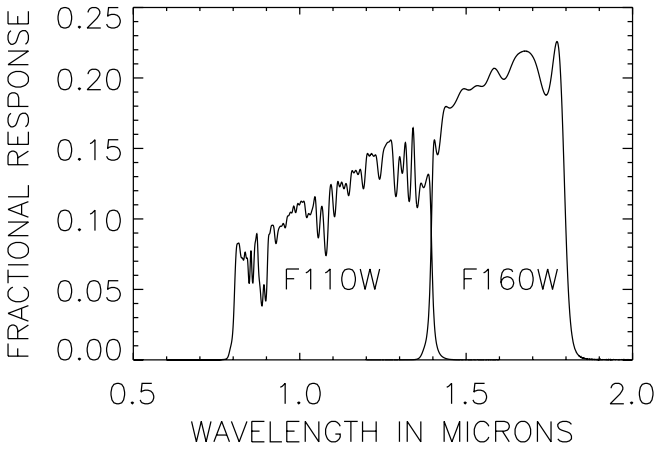

FIG. 1.—Total response functions for the NICMOS F160W and F110W filters. On this plot 100% response is equal to 1.0.

extraction techniques than we have used in producing the Treasury catalog.

2. OBSERVATIONS

The NICMOS observations in the UDF (HST GO/9803) are centered on the position $3^h32^m39\overset{s}{.}0$, $-27°47'29\overset{''}{.}1$ (J2000.0) at approximately the center of the ACS UDF observations.[2] The images lie in a 3×3 grid with centers separated by $45''$. The grid centers are dithered by $5''$ in a 4×4 square pattern tilted at $22\overset{\circ}{.}5$ to the x-axis of the images to reduce the effect of intrapixel sensitivity variations. The tilt of the pattern also produces dithers that have fractional pixel offsets in the detector array.

The NICMOS UDF program consists of 144 orbits broken into two epochs: (1) 2003 August 30–September 14 and (2) 2003 November 2–November 27. The scheduled start of observations in 2003 mid-August was delayed by a safing of the NICMOS Cooling System (NCS) just prior to the beginning of observations. All reference files, such as flats and darks, were obtained subsequent to the safing event. The epochs are separated to enable the detection of Type Ia supernova candidates and to provide enough South Atlantic Anomaly (SAA) crossing-free orbits for high sensitivity. The images in the two epochs are rotated by $90°$ to accommodate the roll restrictions of the spacecraft. In the first epoch the y-axis of the NICMOS camera 3 was oriented $40\overset{\circ}{.}925$ east of north, and in the second epoch it was oriented $130\overset{\circ}{.}925$ east of north. These orientations are the same as the two ACS orientations in an effort to align the NICMOS and ACS images without the need for a rotation. The drizzled ACS images in MAST, however, were produced with the standard north-up, east-left orientation. The version 2 NICMOS Treasury images supplied to MAST are also oriented with north up, unlike the version 1 NICMOS image. The NICMOS version 2 images have been aligned with the ACS version 1 image so that researchers can use the complete set of ACS and NICMOS images without realignment or rotation (see § 3.7).

[2] See image at http://www.stsci.edu/hst/udf/parameters/#Pointing.

Each orbit contains an F110W and F160W band SPARS64, NSAMP = 24, 1344 s integration. Figure 1 shows the total response of the two bands, including the detector quantum efficiency. The F110W integration always precedes the F160W integration. Three orbits comprise a single visit with the location of the image specified by a POSTARG from the central reference position. It is possible that the F160W images from the first orbit of a visit may have received a small amount of earthshine in the last readout of the NSAMP = 24 readout sequence. This is due to the guide star acquisition time on the first orbit of the visit, which takes longer than the guide star reacquisition in the subsequent two orbits of the visit. No correction has been made in the Treasury images for this effect. The 3×3 grid was completed in three visits, with each visit representing a three-image strip stepped in the detector x-direction. The visits were ordered to finish each 3×3 grid before starting another and always in the same order. This was done to maximize the time coverage for a supernova event, should one occur. After the initial delay due to the NCS safing, all the visits occurred in their expected order.

Subsequent analysis of the images indicated that the second-epoch images were not an exact repeat of the first-epoch images. In the second epoch, three of the visits replaced a center image with an image on the right-hand side of the three-image strip. Tables 1 and 2 list the visits, with T, C, and B indicating top, center, and bottom for the first-epoch visits and L, C, and R indicating left, center, and right for the second-epoch visits. These refer to the left, right, top, and bottom of the NICMOS images in their standard x- and y-orientations.

3. DATA REDUCTION

Previous papers (Thompson et al. 1999, 2001; Thompson 2003) described details of the data reduction procedures for deep-field NICMOS observations. Some of the procedures required revision for post-NCS installation data. These changes and the provision of the reduced images as public Treasury program data products warrants a detailed description of the data reduction procedures even though some aspects have been covered in the publications cited above. All the procedures use the commercial Interactive Data Language (IDL)[3] software and the IDL-based Fits List Calculator (FLC; Lytle et al. 1999) software. These procedures were developed primarily by R. I. T. and E. S. for previous NICMOS observations.

3.1. *Basic Reduction*

The initial steps in the data reduction take advantage of the nondestructive readout capability of the NICMOS detectors. NICMOS detectors are read out at specified intervals without erasing or altering the image. This ability allows several data reduction advantages not shared by CCD detectors. The SPARS64 read pattern with 24 samples provides readouts evenly spaced by 63.998 s after the first two samples, which are spaced by 0.303 s. All the images in the NICMOS UDF observations were taken in

[3] IDL is a registered trademark of Research Systems Incorporated, a Kodak company.

TABLE 1
FIRST-EPOCH IMAGE POSITIONS BY VISIT

1	2	3	4	5	6	7	8	9	10	11	12	13	14	15	16	17	18	19	20	21	22	23	24
B	C	T	B	C	T	B	C	T	B	C	T	B	C	T	B	C	T	B	C	T	B	C	T

TABLE 2
Second-Epoch Image Positions by Visit

25	26	27	28	29	30	31	32	33	34	35	36	37	38	39	40	41	42	43	44	45	46	47	48
R	C	L	R	R	L	R	C	L	R	C	L	R	C	L	R	L	C	L	R	R	L	R	R

this mode. The steps described in this section are done automatically in batch processing with no interaction. This is roughly equivalent to the Space Telescope Science Institute (STScI) pipeline processing.

3.1.1. *First Read Subtraction*

The first step in the data reduction is the subtraction of the image obtained in the first read from all subsequent reads. This step eliminates the *kTC* noise that is present in each of the individual photodiodes at the beginning of an integration. The number of reads carried through in the final processing is then 23 reads rather than 24 after this step.

3.1.2. *Dark Current Subtraction*

After the first read subtraction, the dark current image is subtracted from each of the reads. This is a very important step, as the NICMOS detectors have dark current images with very significant structure. This structure is larger in magnitude than the signal from most of the galaxies in the image. The dark images are constructed from integrations in exactly the same mode as the observations but with the cold blank filter in place. This step differs from the STScI pipeline that uses "synthetic darks" calculated from parameters developed during the operation of NICMOS (Mobasher et al. 2004).

3.1.3. *The NICMOS UDF Dark*

The NICMOS UDF dark is a median dark image obtained from dark integrations taken during the Earth occultation period in each of the orbits assigned to the NICMOS UDF program. Operational constraints prevented dark integrations on two orbits, but the remaining 142 dark integrations were used to construct the median images. There is a median dark image for each read constructed from the medians of all the dark images for that particular read.

Between visit 34 and visit 35 of the 48 visits in the NICMOS UDF program, the temperature set point on the NCS was reduced by 0.1 K to compensate for the warmer conditions encountered during the period when the Earth's orbit is closest to the Sun. There was concern that this set point change would alter the nature of the NICMOS darks, since it is known that the darks are temperature-sensitive. Comparison of a median of the darks taken before the set point change with the median darks taken after the set point change did not reveal any differences above the noise level in the observations. The NICMOS UDF dark was therefore constructed from the median of all the darks before and after the set point change.

3.1.4. *Warm Pixels*

In the NCS era the NICMOS detectors operate at a significantly warmer temperature than in the previous operation with solid nitrogen cryogen. There are several advantages to the warmer detector temperature, but a disadvantage is an increase in the number of "hot" and "warm" pixels. Hot pixels are pixels with a dark current high enough to reach the nonlinear response region in a 1000 s integration. These pixels are included in the list of bad pixels described in § 3.1.9. More difficult cases are the warm pixels that have elevated dark current but not elevated enough to become nonlinear in a normal integration. These pixels can be corrected through the dark image subtraction for most types of integrations. The degree of elevation, however, is very temperature-dependent and will vary over the normal range of temperature variations inherent in the NCS operations. The elevated dark current is in many cases much larger than the signal encountered in faint galaxies.

The warm pixels contribute noise in two ways. The first way is the normal Poisson statistics inherent in a steady dark current, and the second way is incomplete removal when the dark current varies from the median dark current measured by the NICMOS UDF dark. The presence of these varying warm pixels altered the previous data reductions in two ways. The first was the introduction of a more aggressive bad pixel list for the UDF observations, and the second was the introduction of postprocessing procedures to detect the presence of warm pixel signals and separate them from true sources. These procedures are described in § 3.6.

3.1.5. *Linearity Correction*

During thermal vacuum testing prior to launch and in cycle 7, the linearity of each pixel was measured. The point at which nonlinearity set in and coefficients for a polynomial fit after that point were determined for every pixel. In the linearity correction stage the signal of every pixel is checked to see if it is in the nonlinear range. If it is above the linear range, its signal is corrected using the determined coefficients of the polynomial fit. If it is in the signal range that is deemed uncorrectable, it is marked as saturated, and only the reads occurring before saturation are used in the analysis. New coefficients are being determined for post-NCS operation. However, none of the galaxies in the UDF reached signal levels requiring correction; therefore, linearity is not an issue in this analysis.

3.1.6. *Cosmic-Ray Removal*

A cosmic-ray event produces a sharp jump in signal intensity in the first readout after the event. Most events do not saturate the pixel, and subsequent readouts continue to monitor the incident flux. At this point in the analysis the readouts are stored as delta signal levels between each readout. The signal "ramp" is reconstructed by adding the delta together. The first step in cosmic-ray detection is a linear fit to the signal ramp, which will be a poor fit to the data if there is a cosmic-ray jump. The residuals to the fit will be increasingly negative with a sharp transition to positive after the event. The cosmic-ray detection procedure looks for the negative-to-positive transition as a signature of a cosmic-ray hit. If it detects a residual transition above the level expected from noise, it removes the delta signal between the two readouts before and after the event, recalculates the signal ramp, and fits a new linear solution.

The cosmic-ray procedure rechecks the ramp to see if there was another cosmic-ray hit and removes the proper delta signal if one is detected. If there is still a detectable cosmic-ray signature after the second refit, the pixel is marked as bad, and no further correction attempt is made. If the signal is saturated after

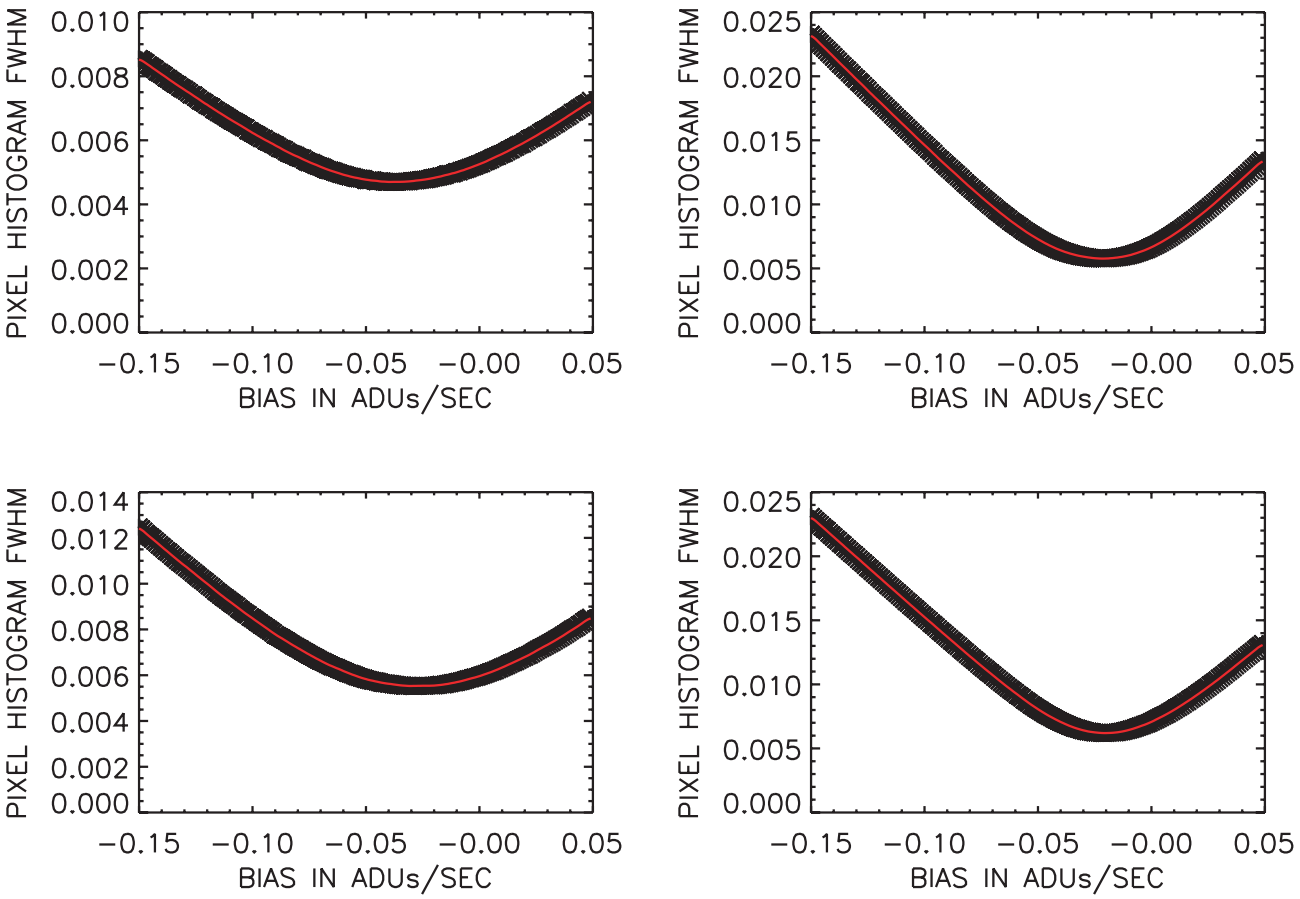

FIG. 2.—Quadrant bias corrections in ADUs per second that produce the minimum variation due to flat-field imprint for one of the NICMOS images. These values are taken as the appropriate quadrant bias correction. The red line shows the polynomial fit to the output, and the black line shows the smoothed fit to the output. In all cases, they completely overlap.

the cosmic-ray hit, only the signal obtained before the event is used in the analysis. The final recorded signal is the value of the slope of the linear fit to the signal ramp in ADUs per second. Cosmic-ray hits that occur in the 0.3 s between the first and second read are detected as fits that do not intercept zero, recalling that the first read is subtracted from the second so that the second read is the first point in the ramp. These hits do not affect the calculated slope but are marked as cosmic-ray hits in the data-quality array discussed later.

3.1.7. *Quadrant Bias Correction*

Each quadrant of the NICMOS detectors has a separate output amplifier to transmit the analog signal to an analog-to-digital converter. This was done to prevent the loss of an entire detector array if there was a failure of an output amplifier. As a side effect of this design decision a small DC bias offset can occur between the four detector quadrants. Although the offset is small, the effect is significant relative to the faint galaxy signals in the UDF and can cause unreliable outputs during the drizzle process. Since there is significant sky background from the zodiacal light, it is difficult to determine the offset amount from a simple inspection of the image.

The quadrant bias is removed via a procedure based on the bias removal procedure developed by M. Dickinson as part of the STScI NICMOS team (Mobasher et al. 2004). The procedure uses the flat-field imprint produced on the DC signal by the flat-field correction process. Any flat DC bias will be modulated by the variations in the flat field. The process successively subtracts a DC bias from each quadrant before it is flat-fielded, applies the flat field, and then picks the bias subtraction that produces the minimum variation in the quadrant. The variation in the quadrant signal is measured by a Gaussian fitting to the histogram of pixel values in the images. To avoid any residual corner glow from the amplifiers or other quadrant boundary anomalies, only the quadrant region that is at least 20 pixels from the quadrant edges is used to determine the quadrant bias. Bad pixels are also masked out to prevent them from dominating the variation signal. The output of variations from each bias correction is fit by both a second-order polynomial and by five-point smoothing of the output. In the cases encountered in the UDF images, they are essentially identical. The minimum variation bias correction is selected as the minimum of the smoothed output.

Both positive and negative bias are subtracted, as the bias can have either a positive or negative value. The bias subtraction used biases between -0.15 and 0.2 ADUs s^{-1} incremented in 0.001 ADUs s^{-1}. The procedure returns a warning if any bias corrections do not find a minimum in the provided range of biases. All the UDF quadrant images had minimums within the range of biases in the procedure. An example of the Gaussian width versus subtracted bias is shown in Figure 2. Visual inspection of the images before and after background subtraction confirmed that there were no detectable remaining quadrant bias offsets. The procedure would be unnecessarily time-consuming for images in which the objects were significantly brighter than the offsets and might not work in images in which the width of

the pixel signal histograms is dominated by source variations rather than noise. Neither is the case for the UDF. In reality the IDL code for this procedure actually performs both the flat-fielding and bad-pixel correction. These procedures, however, are discussed individually in the following sections.

3.1.8. *Flat-Fielding*

NICMOS flat fields are created internally. The "beam steering mirror" internal to the instrument lies at an optical pupil and is used to correct the spherical aberration of the *HST* primary. It can be illuminated from behind, and the reflective coating of the mirror was adjusted to be about 0.01% transmissive, producing an illuminated pupil for flat-fielding. Flat fields are produced at regular intervals during operation in all filters of each camera. We used F110W and F160W camera 3 flat-field observations created on 2003 September 9 from proposal 9640. The flat fields are analyzed in the identical manner as described in the preceding steps. The STScI reference flat fields were not used in this analysis because they were based on flat fields observed previous to the NCS safing event.

One of the effects that the flat field corrects is a slight vignetting along the lower edge of camera 3. For two reasons this correction was not effective in the UDF fields. First, the net effect has two components, vignetting of the incoming astronomical flux and emission from the vignetting component, which is thought to be the edge of the mount for the field division mirror for camera 3. For bright sources the vignetting is the dominant effect, and the flat field properly corrects the field. For very faint images, such as the UDF, emission can be a significant component that varies due to the natural temperature variations in the aft shroud. Second, variations in geometry due to temperature changes can affect the degree of vignetting. Again, the effect is slight for bright sources but can be significant for the UDF signal levels. For these reasons the lower 20 rows of all UDF images were masked off in the drizzle procedure described in § 3.7.

3.1.9. *Bad Pixel Correction*

Bad pixels are defined as pixels with quantum efficiencies (QEs) of less than 10% of the average QE or with dark currents high enough to reach nonlinear signal levels in 1000 s or less. In the post-NCS era the list of bad pixels has increased over the cycle 7 listing due to the higher temperature of the detector creating more high dark current pixels. Pixels that satisfy neither criterion but are highly variable in their dark current were also added to the list. All bad pixel signals are replaced with the median of the 8 pixels surrounding them. In the case of adjacent bad pixels, that number is reduced by the number of adjoining bad pixels. All bad pixels are listed in the data-quality array, which is an extension of the image or science array. Table 3 gives the decimal codes for each of the steps described above. They are each a single, different, binary bit, so each combination of actions performed on a pixel has a unique output code. Note that only a few of the 16 bits available for pixel actions are used in this analysis. A full set of data-quality codes can be found in the NICMOS Handbook, but only the ones listed here are used in the NICMOS UDF Treasury data. Even for the codes used, they may in many cases differ from the codes returned by the STScI pipeline analysis. As an example, the lists of bad pixels differ between the pipeline analysis and the analysis described here. Note that the data-quality extensions only exist for the individual NICMOS UDF images. The drizzle procedure does not preserve these codes, since many input pixels contribute to a single drizzled output pixel.

TABLE 3
Data-Quality Codes

Bit or Number	Bad Pixel	Cosmic Ray	Nonlinear	Saturated
Bit	8	9	12	13
Number	256	512	4096	8192

3.2. *SAA Persistence Correction*

The program planners at STScI were careful to schedule the NICMOS UDF observations in orbits that were not impacted by SAA passages. None of the NICMOS UDF images required any correction to remove SAA persistence.

3.3. *Earthshine Detection*

As mentioned in § 2, the last read of the first orbit in a visit may have encountered increased earthshine due to the longer period of delay in a guide star acquisition than in a reacquisition. This would only affect the F160W images, as the readout sequence was always F110W and then F160W. We tested for this effect by plotting the median of the delta increase in the F160W images as a function of readout. In a few cases we saw a detectable rise in the last readout of the first orbit in a visit. The effect appeared minor enough that no correction was attempted.

3.4. *Background Subtraction*

The primary background source in the UDF is zodiacal emission, which is relatively uniform across the small UDF field of view. A median image of all the images in the F110W filter and in the F160W filter determines the background for that filter. The background is simply subtracted from each image in the proper filter. The median image is extremely smooth, with no indication of any residual source structure. This is similar to the results in the Hubble Deep Field-North (HDF-N; Thompson et al. 1999), in which the spacing between images was much smaller than in the UDF. Since the zodiacal backgrounds can be time-dependent, the first-epoch and second-epoch background subtractions were done independently.

3.5. *Residual Bias Correction*

The removal of quadrant biases and the background subtraction should result in an image that has a median value of nearly zero, since most of the pixels in the image are not in sources that are above the noise level. The minimums of the quadrant bias curves in Figure 2, however, are rather broad. To compensate for this, each quadrant of every image was set to zero bias. The bias was determined from the median of the portion of the quadrants that is 40 rows and columns away from the edge to avoid any contamination from residual corner glow or uncorrected vignetting. Any detected bias was subtracted from the entire quadrant to produce a zero-bias image. Inspection by eye of the zero-bias images did not find any detectable quadrant offsets.

3.6. *Warm Pixel Correction*

A new effect encountered in the NICMOS UDF images is warm pixel variation. At the higher operating temperature of the NCS, the NICMOS detectors have more warm pixels than during the cycle 7 operation with solid nitrogen cryogen. A warm pixel is defined as a pixel with an elevated dark current that is not high enough to be declared a bad pixel by the criteria defined in § 3.1.9. For most applications warm pixels are adequately

TABLE 4
NICMOS Camera 3 Distortion Coefficients

x or y	1	2	3	4	5	6	7	8	9	10
x	0.0	1.0014705	0.0	8.0317971E−6	1.3219373E−5	5.8285553E−6	0.0	0.0	0.0	0.0
y	0.0	−8.9368516E−4	0.99853067	−1.8073393E−5	0.59911861E−7	−1.1582927E−5	0.0	0.0	0.0	0.0

corrected by dark subtraction, but for the UDF they present two problems. The first problem is that their dark current is temperature-sensitive, and the NCS has slight temperature variations within an orbital cycle and within a 24 hr day due to power cycles in *HST* operation. The variation is small but significant relative to faint UDF sources. The second problem is that the Poisson noise of the signal at the end of an integration is also significant relative to a UDF source. The individual images have single or sometimes double pixels with signal levels of either positive or negative high contrast relative to the surrounding pixels from the warm pixel effect.

Warm pixels are identified by their contrast with neighboring pixels. The point-spread function (PSF) of a point source centered on a pixel provides a maximum contrast for a real source. Pixels with contrasts significantly greater than this are due to warm pixels. The contrast was computed for each pixel compared to the 8 pixels adjacent to it. A pixel is set equal to the median of the 8 pixels if three conditions are met: (1) its value is higher than the 3 σ noise value in the image, (2) its value is higher relative to the median of the adjacent pixels than a preset contrast value, and (3) the value of the surrounding median is less than a preset number of standard deviations. The last condition prevents peak clipping on point objects. The contrast values were set to 6.0 for the F160W image and 8.0 for the F110W image, which has a narrower PSF. The standard deviation limits were set to 2.5 for the F160W images and 2.0 for the F110W images. Any corrected pixel has the bad pixel flag set in the data-quality image extension so it can be identified.

3.7. *Drizzle Procedure*

The Treasury mosaic images were produced using the drizzle procedure with context images (Fruchter & Hook 2002). The offsets for the NICMOS images were determined by registering the NICMOS F110W images onto the ACS F850LP UDF image in the *HST* archive, which has a north-up orientation and 0.″03 pixel scale. The significant overlap between the two filters greatly reduces any errors due to color-dependent morphology; however, see § 3.7.3 for an assessment of the accuracy of the alignment. The NICMOS F160W images, which always immediately followed the F110W images in an orbit, were assumed to have the same offset as the F110W images preceding them. The ACS image was reduced to 0.″09 pixels by a simple 3×3 pixel^2 addition of the image. Individual NICMOS F110W images were then produced with a drizzle PIXFRAC parameter of 0.6 and a SCALE parameter of 0.09/0.202863 to produce 0.″09 output pixels. The denominator in the scale factor is the pixel size of the distortion-corrected NICMOS pixel. The geometric distortion coefficients (L. Bergeron 2004, private communication) are given in Table 4. These coefficients are the constants for a cubic distortion correction of the form

$$x_{\rm dist} = a_1 + a_2 x + a_3 y + a_5 xy + a_6 y^2 + a_7 x^3 + a_8 x^2 y + a_9 x y^3 \quad (1)$$

and an identical equation in b coefficients for the y position that governs the placement of the pixels. Compared to other *HST* instruments the correction is relatively small. The main component is the difference in plate scale between the x- and y-directions due to a slight tilt in the camera 3 focal plane relative to the plane of the detector. The tilt is due to the curvature of the focal plane. Each 0.″09 NICMOS image was rotated to a north-up orientation using the ORIENTAT value in the image header.

A three-step process provided the positions of each F110W image relative to the ACS F850LP image. The first step was to shift the NICMOS images to the positions indicated by their world coordinate system positions in the headers. The second step was a noninteractive χ^2 minimization of the differences between the bright objects in the NICMOS image and the nearest corresponding bright ACS object. The ACS positions were determined with the source extraction program SExtractor (SE) in the ABSOLUTE mode with the threshold set at 0.03 ADU s^{-1}. Positions in the NICMOS images were also determined with SE in ABSOLUTE mode with the threshold set at 0.01 ADU s^{-1}. Both of these thresholds are quite bright in order to ensure a low source count per area. This made the likelihood of wrong object-matching low. The shifts were limited to ± 10 pixels in the x- and y-directions in single-pixel steps. The average position shift in this step was on the order of 2–3 0.″09 pixels. The final shifts were determined by a similar χ^2 minimization of interactively selected NICMOS objects. Usually three objects were selected on the basis of compact size and sufficient signal-to-noise ratio. Whenever fully visible in a NICMOS image, the star near the center of the image was used as one of the objects. The more eastern star image appears to have contamination due to a faint nearby object visible in the ACS images. Shifts in this step were limited to ± 1 pixel in 0.1 pixel steps. The average position adjustment in this third and final stage was 0.2–0.3 0.″09 pixels. These final positions were then used as the input to the drizzle procedure.

3.7.1. *Individual Image Masking*

The F110W and F160W images each have a general mask used in the drizzle process. These mask out the bottom 20 rows of the image to eliminate the partially vignetted region at the bottom of camera 3. They also mask out a portion of the upper right-hand corner of camera 3 where there is an area of rapidly changing QE. In addition, they also mask out the known bad pixels and areas in which some particles, termed "grot," cover detector pixels. The large number of dithered images greatly reduces the impact of the masked areas. The masks are available in the STScI NICMOS UDF Treasury version 2.0 archive in MAST. Several of the images had artifacts, such as satellite passage streaks, that required masking. Individual masks were made for 20 F110W images and 31 F160W images. Table 5 lists the masked images. The masks are contained in the NICMOS version 2.0 Treasury submission.

3.7.2. *Cosmic-Ray Persistence*

A few of the masks remove spurious objects created by cosmic-ray persistence. If a cosmic-ray hit before the start of an integration produces a shower of particles, cosmic-ray persistence

TABLE 5
IMAGES WITH SPECIAL MASKS

F110W	F160W
01bl	01ct
08me	03jy
09tf	03kj
13ap	06et
18c3	07ka
20j6	13au
27es	14d1
28im	14dn
29jr	16ve
30wj	17b8
32xe	20jb
33fh	25c4
34m8	26cm
34mq	27f0
35nt	28jc
36ot	28l1
38zd	29l1
40qs	31vp
44js	32xl
45qg	34my
...	35ny
...	36nx
...	36p0
...	38zk
...	39pe
...	40pw
...	42ht
...	43i7
...	44jz
...	45rl
...	48az

NOTE.—The numbers and letters are the unique sections of the file names.

can give a resolved source that appears in the first F110W image after the hit and more weakly in the following F160W image. This exactly mimics a high-redshift galaxy. The ACS image has no signal, and the F110W-F160W color is blue. The signature of this spurious event is that the source only appears in one set of F110W and F160W images. All the NICMOS sources that did not have ACS counterparts were inspected in each image. Two spurious cosmic-ray persistence sources were found and masked out (see also § 7.4).

3.7.3. *Point-Spread Functions*

Unlike the deep NICMOS observations in the HDF-N, the *HST* secondary mirror was not adjusted to bring the camera 3 images into sharp focus. The photometric gain was not considered high enough to request the adjustment, which would have put the parallel ACS images significantly out of focus. The PSF at the focal plane of camera 3 is therefore broader than the diffraction-limited PSF observed by NICMOS cameras 1 and 2. To determine the PSFs of the UDF images, two measurements were performed. The first was to measure the PSF of the bright star at $x = 1897.26,\ y = 1610.34$ with Gaussian fitting. The second bright star at $x = 1246.12,\ y = 1420.42$ appears to be double with a faint companion. The second measurement involved 42 camera 3 images in F110W and F160W of the photometric calibration star P330-E taken after the NCS safing event. These were part of the proposal 9995 calibration program of M. Dickinson. These images were drizzled in the same manner as the UDF images. The PSFs of the drizzled F110W and F160W images were measured by the same Gaussian fitting as for the UDF stellar images. The results are listed in Table 6, which gives the measured major- and minor-axis FWHM values. Table 6 also gives the results of performing the same exercise on synthetic images produced with the Tiny Tim software (Krist & Hook 2004)[4] for the camera 3 focus used in the UDF observations. The Tiny Tim and calibration star PSFs agree quite well, but the measured UDF stellar values are between 0.″06 and 0.″1 wider. This may reflect the accuracy of the mosaic position calculations. The widths measured in an independently reduced image (see § 7.4) are very similar to our UDF image widths. Any researcher that requires extremely accurate object shapes, such as for weak lensing, may wish to go to the original single images for size and shape measurements. Those researchers should apply the geometric distortion corrections listed in Table 4.

4. IMAGE SIZE AND WEIGHT

The full drizzled image does not have a uniform integration time over the image. In particular, the edges of the image have only one integration, as opposed to the average 16 integrations for the interior of the image. The full drizzled image has a size of 3500×3500 pixels, the same size and orientation as the ACS images reduced to 0.″09 pixels. Experience with the HDF-N images indicated that source extraction in regions with less than half of the average integration time was not profitable, except in special cases in which a particular object near the edge of the total image required analysis. Users of the Treasury image should be aware that the edges of the image have a roughly $\sqrt{2}$ lower signal-to-noise ratio than the central regions. The exact weight for all pixels is given by the weight images included in the Treasury archive. There are some regions in which the images overlap that have much higher integration times. Users who

[4] The Tiny Tim software and manual are available at http://www.stsci.edu/software/tinytim.

TABLE 6
OBSERVED PSF PARAMETERS

	UDF STAR (arcsec)		UDF STAR[a] (arcsec)		P330-E (arcsec)		TINY TIM (arcsec)	
PARAMETER	F110W	F160W	F110W	F160W	F110W	F160W	F110W	F160W
FWHM major	0.36	0.39	0.38	0.38	0.29	0.30	0.29	0.27
FWHM minor	0.32	0.36	0.35	0.35	0.26	0.26	0.25	0.24

NOTE.—The observed PSF parameters are given for the star in the NICMOS UDF images at (x, y) (819.2, 597.3), a calibration star P330-E drizzled in the same way as the UDF images, and a synthetic Tiny Tim image at the camera 3 focal position used in the UDF.

[a] These values were measured for the images kindly supplied by M. Stiavelli, B. Mobasher, and L. Bergeron. See § 7.4.

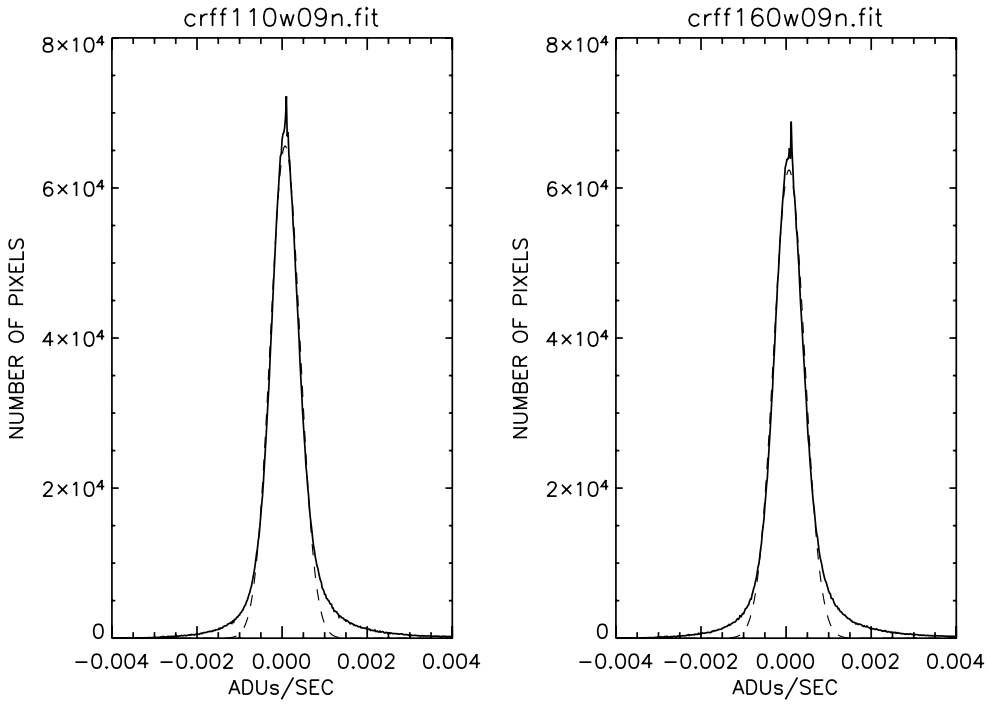

FIG. 3.—Histograms of the pixel values in the F110W (*left*) and F160W (*right*) images. The deviation from the Gaussian fit on the positive side is due to the contribution of sources. The width of the Gaussian is an indication of the noise in the images. See § 5.1 for a discussion of the pixel noise.

need a uniform selection criterion for analysis should be aware of these differences in weight.

5. SOURCE EXTRACTION

Source extraction in the science image was performed with SE version 2.3 (Bertin & Arnout 1996) in the dual image and rms image modes. The source extraction included the four ACS UDF images, as well as the NICMOS images. The ACS extractions provided the source reality check described in § 7.3 and are included in the Treasury catalog.

5.1. *Noise*

Figure 3 shows the histograms of all the pixel values in the F110W and F160W images. The majority of the pixels are well fit with a Gaussian centered on zero. The offsets from zero are 7×10^{-5} ADU s^{-1} for both images. The positive tail deviating from a Gaussian is the contribution from the true sources in the field. The width of the Gaussian fit is an indicator of the noise. The Gaussian fit gives noise levels of 3.5×10^{-4} ADU s^{-1} for the F110W image and 3.7×10^{-4} ADU s^{-1} for the F160W image. This corresponds to 0.55 and 0.58 nJy, respectively. This is an underestimate of the true noise, as is partially indicated by the excess over the Gaussian on the negative side of the fit. The drizzle procedure is known to introduce correlation to the noise (Fruchter & Hook 2002). Fruchter & Hook (2002) give an expression for the noise increase factor that gives a factor of 1.8 for the drizzle PIXFRAC and SCALE parameters used in the images. This yields 1 σ noise values of 1.0 and 1.2 nJy pixel^{-1}.

Figure 4 shows the histograms of the signals in a densely packed grid of apertures of the same diameter as the three apertures (6, 11, and 17 pixels) used in the source extraction. The 175×175 grid is regularly spaced on 20 pixel centers to provide 30,625 apertures. Most of these do not contain sources, but the positive tail in Figure 4 indicates apertures with positive source flux. The large number of apertures that fall off the NICMOS image are not included in the analysis. The histograms are roughly Gaussian-shaped, but only the 6 pixel aperture histogram has an easily measurable FWHM. The 1 σ noise derived from the FWHM is 3.7×10^{-3} ADUs s^{-1} for the F110W image. Similar results were obtained for the F160W image. The expected noise from the individual pixel noise described above, including the factor of 1.8, is 3.5×10^{-3}, which is comparable to the measured value. To the degree that the aperture noises are truly Gaussian-distributed, this indicates that a factor of 1.8 is a reasonable figure to account for the correlated noise and that the aperture noise is approximately equal to the square root of the number of pixels in the aperture times the individual pixel noise. The measured aperture noise in janskys from the histogram is 5.8×10^{-9}, which is equivalent to an AB magnitude of 29.5 for the 0.″54 diameter aperture. The

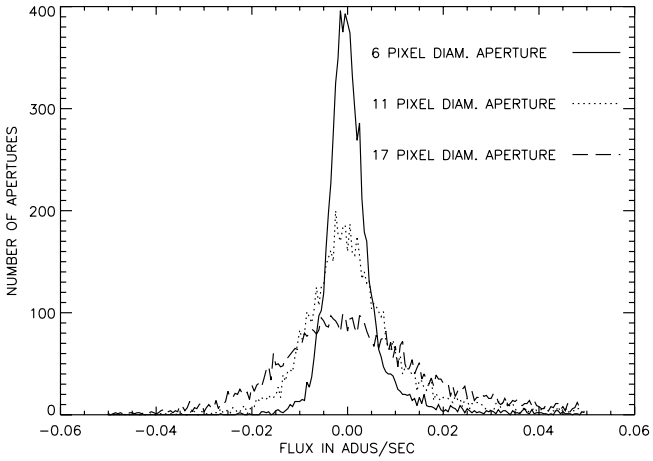

FIG. 4.—Histograms of the flux in a densely packed grid of apertures covering the UDF F110W image. The three apertures are 6, 11, and 17 pixels wide. See § 5.1 for a discussion of the aperture noise.

5 σ AB magnitude is 27.7, which we take as the appropriate value independent of source noise. In observations of the HDF-S, Labbé et al. (2003), with the Infrared Spectrometer and Array Camera on the VLT, found 1 σ aperture noises of 28.6 and 28.1 for the J and H bands with a 0.″7 diameter aperture, which gives 5 σ values of 26.7 and 26.2. The minimum number of contiguous pixels for a real source is set to seven in the extraction procedure. The 5 σ noise for a point-source detection is then the noise in the 7 pixel aperture, which gives AB magnitudes of 30.35 and 30.15 for the F110W and F160W filters, respectively.

5.2. *Detection Image*

In the two-image mode SE uses a detection image to determine the position and extent of sources. The individual image source extraction is then performed on exactly the same positions and regions determined from the detection image. The SE parameters regarding source geometry such as area and ellipticity are determined by the detection image. The detection image for the Treasury catalog is the simple sum of the F110W and F160W science images. Even though it is the sum of two images, the detection image has a significantly lower signal-to-noise ratio than any of the ACS UDF images, except for sources that are extremely red. Users that are interested in the NICMOS limits on faint ACS UDF sources should use the ACS images as the detection images to perform the source extraction on the NICMOS images. On the other hand, very red sources may appear only in the NICMOS images. Since we wish to provide an infrared catalog, we choose to use the NICMOS images for extraction. Note that by combining the two NICMOS images there is a bias against the very reddest sources that might only appear in the F160W image.

5.3. *rms Image*

SE uses an rms image to determine the detection limit of a pixel signal when operating in the rms mode used in the Treasury version 2.0 catalog. The drizzle procedure produces an observation time weight map that measures the total integration time for every pixel, but the weight map does not take into account the large variations in QE over the face of the NICMOS detector array. To account for the QE variations, the F110W and F160W flat-field images were drizzled in exactly the same way as the UDF images, using identical masks. Note that the flat-field images are the multiplicative flats used in the normal image reductions. As such, they are high where the signal is low and vice versa. All subsequent postdrizzle procedures that were applied to the science images were also applied to the drizzled flat images. Next the median of the drizzled flat images was set to one and multiplied by the standard deviation determined in § 5.1, adjusted by the correlation parameter of 1.8. These images were then added together as the square root of the sum of the squares to form the rms image for the detection image supplied to SE. This rms image properly represents the differences in QE across the detector and the mapping of the differences onto the final science image. The individual F110W and F160W rms images were retained for use in the source extraction described below. The ACS rms images were assumed to be uniform and equal to the standard deviations found in § 5.1 for the individual ACS images. The individual filter rms images form the basis of the magnitude and flux errors returned by SE.

5.3.1. *rms Image Adjustments*

Visual inspection of the detection image and the individual NICMOS drizzled images revealed small areas in which there were clearly higher regions of noise or residual spurious artifacts. These are usually regions of ''cross-hatched'' noise or small irregular regions of a few pixels with boundaries too sharp to be real sources. Even though areas such as these were masked in the original images, the drizzle process can produce additional areas due to the rebinning process. Rather than removing these regions from the images, the rms images were adjusted to guarantee that they were not used in the source extraction. The pixel regions with adjusted rms values are given in a table supplied with the version 2 submission to MAST. These regions can also be identified in the rms images themselves, where they have been set to 9.999. This procedure preserves the ignored areas in the images so that they can be evaluated by other researchers if they wish, just as the individual images, before masking, can be retrieved from the archive. Areas outside of the observed regions were set to very high rms values on the order of 500–800.

TABLE 7

Source Extraction Parameters Used in the NICMOS Treasury Version 2.0 Catalog

Parameter	Value
THRESH_TYPE	RELATIVE
ANALYSIS_THRESH	1.4
DEBLEND_NTHRESH	32
CLEAN_PARAM	5
WEIGHT_TYPE	RMS_WEIGHT
DETECT_MINAREA	7
FILTER	Y
DEBLEND_MINCONT	0.001
MASK_TYPE	CORRECT
PHOT_APERTURES	6, 11, 17
DETECT_THRESH	1.4
FILTER_NAME	detec.conv
CLEAN	Y
WEIGHT_IMAGE	rms_combfix.fit, rmsfilter.fit
PHOT_AUTOPARAMS	2.5, 3.5

Notes.—Obvious parameters such as DETECT_TYPE = CCD have not been entered. The full configuration files are part of the ver. 2.0 Treasury archive in MAST. rmsfilter.fit refers to the rms image for a given filter, such as rmsF160W.fit.

5.4. *Extraction Parameters*

SE's source extraction process is controlled by a configuration file that gives the parameters for source extraction. Some of the configuration parameters used in the version 2.0 Treasury source extraction are given in Table 7. The full configuration files used in the extraction are included in the Treasury NICMOS UDF version 2.0 submission to MAST. The parameters include a detection threshold of 1.4 σ and the minimum number of contiguous pixels for a true source set to seven. Note that these parameters discriminate against faint point sources.

Although not evident from the documentation, SE runs in a dual rms image mode. In this mode two rms images are supplied in the WEIGHT_IMAGE parameter. The first image is the rms image for the detection image; the second is the rms image for the extraction image, which is the UDF image in each of the individual filters. The second rms image does not influence the source selection but determines the error values returned by SE.

The photometric zero points in AB magnitude are 23.41 (F110W) and 23.22 (F160W). The extraction parameters were adjusted to produce a clean extraction of sources with a goal of no erroneous detections in the high signal-to-noise ratio regions of the image. This produces a relatively conservative catalog

TABLE 8
A Minicatalog of Source Parameters

ID (1)	ACS (2)	Seg. (3)	x (4)	y (5)	R.A. (6)	Decl. (7)	P.A. (8)	Ellipticity (9)	R_h (10)	FWHM (11)	Stellarity (12)
1	4394	605	2877.54	1797.00	53.13059235	−27.79026222	0.0000	0.8470	2.9450	4.3800	0.840
2	5109	631	2789.20	1766.72	53.13309097	−27.79101944	−23.9000	0.1540	2.0870	7.1800	0.890
3	5010	636	2764.20	1762.93	53.13379669	−27.79111481	78.0000	0.5340	4.0370	8.7800	0.910
4	4638	702	2750.66	1709.68	53.13417816	−27.79244423	−45.3000	0.4250	2.8050	5.6200	0.700
5	3460	926	2697.05	1500.98	53.13569260	−27.79766273	45.3000	0.4080	3.3700	4.1400	0.730
6	5115	627	2685.79	1769.54	53.13601303	−27.79094887	27.4000	0.3890	2.9230	7.2000	0.920
7	3871	842	2673.44	1586.07	53.13636017	−27.79553413	68.7000	0.4570	3.9490	9.2400	0.520
8	4350	774	2671.81	1643.54	53.13640594	−27.79409790	−21.0000	0.0550	2.8130	5.1000	0.980
9	3938	867	2666.78	1572.05	53.13655090	−27.79588509	17.7000	0.0380	2.5200	4.1100	0.940
10	4370	792	2661.00	1637.50	53.13671112	−27.79424858	89.8000	0.1730	2.7700	4.6100	0.430

Notes.—Table 8 is published in its entirety in the electronic edition of *The Astronomical Journal*. A portion is shown here for guidance regarding its form and content. See § 6.1 for a description of the parameters.

given the range of weighting over the image. Visual inspection of the image indicates that there are real sources that have been missed by the extraction process. More aggressive extraction parameters pick up these sources but also begin to find sources of doubtful reality (see § 7). Users who wish to have a more aggressive extraction can use our parameters as a starting point and adjust them to produce the required level of extraction. Our parameters produced 1293 extracted sources.

6. CATALOG CONSTRUCTION

All the output values listed in the Treasury catalog are outputs from SE with no editing. The source order has been rearranged to be in order of increasing right ascension. To maintain correspondence with the segmentation images that were returned by SE, the original source identification numbers assigned by SE are given in the catalog. Ten of the sources detected by SE are not included in the catalog as described in § 7.3, leaving 1283 of the 1293 detected sources.

Each source has 90 entries; therefore, we do not include the table in this paper. The catalog is available at the STScI MAST Web site containing the NICMOS version 2.0 high-level science products. That catalog is a comma-separated text file. Columns (1) and (2) contain the identification number and the identification number of the associated source in the version 1 *I*-band-based ACS UDF catalog. The associated ACS source is the closest source to the catalog source. If there is no ACS source within 0.3 s of the NICMOS source, a "0" entry is made in column (2). Column (3) gives the distance to the associated source in arcseconds, and column (4) gives the identification number of the source in the SE-produced segmentation image, which is also provided in the MAST archive. If a version 2 catalog of ACS sources is produced, we will attempt to provide a version 2.1 catalog with the new ACS source identifications included.

Columns (5) and (6) give the x- and y-positions in pixels of the source in the version 2.0 Treasury image. Columns (7) and (8) are the right ascension and declination positions in degrees, while columns (9) and (10) are the right ascension and declination positions in traditional nomenclature. Columns (11)–(28) give the aperture AB magnitudes of the source. The three aperture magnitudes of the ACS F445W band are listed first, followed by the remaining ACS and NICMOS bands in order of wavelength. Columns (29)–(34) list the isophotal magnitudes, and columns (35)–(40) list auto magnitudes returned by SE in the same order.

Column (41) lists the number of pixels associated with the source in the SE segmentation image. Columns (42)–(47) list the FWHM in each band. Column (48) lists the position angle of the source returned by SE. Column (49) lists the flag value returned by SE. No sources have been removed from the catalog on the basis of the value of the SE error flag. Columns (50)–(55) list the XPEAK, YPEAK, XMIN, YMIN, XMAX, and YMAX values returned by SE. The source is contained in a box defined by the minimum and maximum x- and y-values. Columns (56) and (57) give the ellipticity and elongation of the source returned by SE. Column (58) contains the 0.″6 diameter aperture AB magnitude of the F160W band.

Columns (59)–(76) contain the aperture fluxes in the same order as the aperture magnitudes. The fluxes are in ADUs per second. The NICMOS gain is 6.5 electrons per ADU. Columns (77)–(82) list the isophotal fluxes, and columns (83)–(88) list auto fluxes returned by SE. Columns (89) and (90) are the ISOAREA and ISOFAREA values returned by SE.

6.1. *Minicatalog*

To be consistent with the ACS UDF submissions, we have also constructed a minicatalog of the sources, part of which is included in the printed version of this paper. The whole catalog is available in the electronic version of this paper. The catalog appears in Table 8. There are some differences relative to the ACS catalog available in MAST. First, the catalog is ordered in right ascension with the associated ACS source identification and the segmentation identification in columns (2) and (3). The x- and y-positions followed by the right ascension and declination in degrees are in columns (4)–(7). Next are the position angle, ellipticity, half-radius, FWHM, and stellarity in columns (8)–(12). These are followed by the isophotal magnitude, isophotal magnitude error, and signal-to-noise ratio for the four ACS and two NICMOS bands, starting with the ACS F435W and ending with the NICMOS F160W band. The signal-to-noise ratio is the ratio of the isophotal flux to the isophotal flux error returned by SE. The last column in the table is the value of the error flag returned by SE. As in the larger table there has been no effort to remove sources based on the SE error flag. Due to space constraints, only the first few columns of the table are present in the printed version.

7. SOURCE RELIABILITY

Although the extraction parameters were adjusted conservatively, independent assessments of the source reliability are

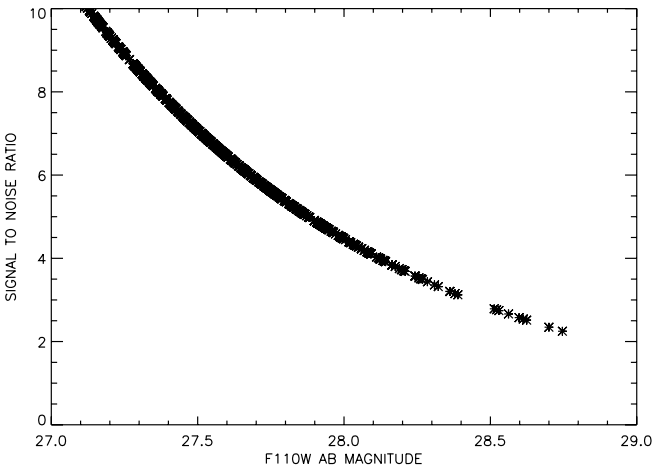

FIG. 5.—Faint end of the isophotal F110W AB magnitude versus signal-to-noise ratio plot, where the signal-to-noise ratio is calculated from the isophotal flux and isophotal flux error returned by SE. Each source is marked by an asterisk. In general, the flux error returned by SE is smaller than that calculated by other means. See the discussion in § 7.1.

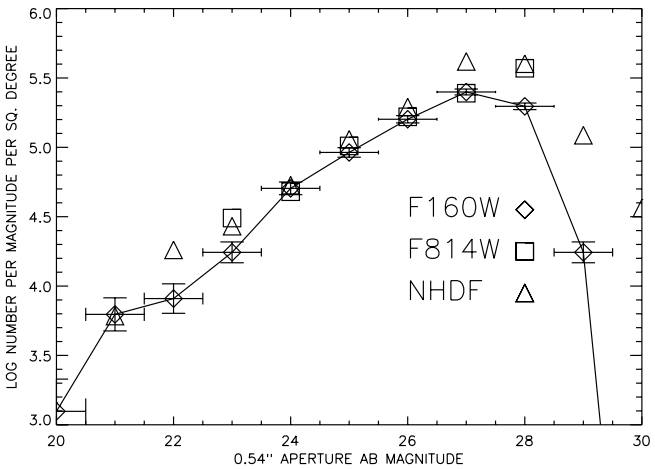

FIG. 6.—*H*-band (F160W) number-magnitude diagram for the UDF. The error bars are strictly due to number statistics and do not reflect completeness or systematic errors. For comparison, the HDF-N F814W and F160W data are overplotted. The falloff at AB magnitudes greater than 27 is partially due to the conservative nature of the source extraction used for the Treasury ver. 2.0 catalog.

required. The following analyses and tests were performed to judge the reality of the catalog sources.

7.1. *Signal-to-Noise Ratio Values*

The source extraction program, SE, returns flux errors as well as fluxes. Figure 5 shows the measured signal-to-noise ratio values for the faint end of the catalog. The ratio of the isophotal flux to isophotal flux error is plotted versus isophotal magnitude. There is significant scatter in the values, as expected. The average magnitude for a signal-to-noise ratio of 5 appears to be around an isophotal magnitude of 28.4, significantly fainter than the aperture test value of 27.7 found in § 5.1. The details of how SE computes its flux errors are not immediately obvious, so the value of 27.7 is used. The rms images supplied to SE were multiplied by 1.8 for the expected correlation due to drizzling, so that should not be an explanation for the difference.

7.2. *Negative Image*

As a check on noise-induced sources, we ran the identical extraction procedure on the negative of the original source detection image. The procedure produced no detections from the negative image. This indicates that the number of sources produced by noise is very low.

7.3. *Comparison with the ACS Images*

The presence of the much higher signal-to-noise ratio ACS images provided a second test of source reliability. We checked for catalog sources that had ACS F850LP 0.″6 aperture diameter AB magnitudes fainter than 29.5. The smallest aperture was chosen to minimize flux from overlapping sources. We identified 22 sources out of the total 1293 sources that matched that criterion. Two of these sources are in the high-redshift source list of five sources described by Bouwens et al. (2004) in which the Lyman break occurs to the red of the ACS cutoff. Bouwens et al. (2004) used a more aggressive source extraction, which accounts for the extra three sources in their analysis. The remaining 20 sources fell into three categories. The first category is legitimate sources with ACS F850LP flux below the limit but clearly there under visual inspection. There are 10 sources in this category. The second category is sources with clear flux in only the F160W band. There are two sources in this category. The remaining eight were sources that appear to be noise artifacts by a subjective visual analysis. The 10 objects in the last two categories do not appear in the catalog even though the two sources with only F160W flux may be real.

7.4. *Comparison with an Independently Generated Image*

The NICMOS UDF images were independently reduced at STScI by M. Stiavelli, B. Mobasher, and L. Bergeron. They very graciously provided these images for comparison with our reductions. Inspection of these images revealed two objects in our images that were the result of cosmic-ray persistence (see § 3.7.2). These objects were masked out in the individual image they appeared in for the final drizzle run. One NICMOS object that does not have an ACS counterpart, object 937 (UDF 818-886; Bouwens et al. 2004), does not appear in the image from Stiavelli, Mobasher, and Bergeron. Inspection of our individual images indicates that no single image contributed the majority of the flux, as would be expected for a cosmic-ray persistence event. The object appears faintly in several of our individual images in both filters. To date we have not been able to resolve why this discrepancy exists. Users of the catalog should be aware of this discrepancy, particularly because this source satisfies the criteria for a galaxy at a redshift greater than 7.

8. CONCLUSIONS

Although this is a description of the data and techniques used in constructing the NICMOS UDF Treasury version 2.0 catalog, it has been traditional (Williams et al. 1996; Thompson et al. 1999) to show a number-magnitude diagram from the data. Figure 6 displays the number-magnitude diagram in AB magnitudes for the NICMOS F160W sources in the Ultra Deep Field. The vertical error bars are calculated from number statistics only. Other errors, such as incompleteness, source noise, and large-scale structure, are not included. The falloff at AB magnitudes greater than 27 is certainly due to incompleteness, partially due to the conservative source extraction parameters used in the construction of the Treasury catalog. Note that the magnitudes are aperture magnitudes in the smallest, 0.″6, aperture. For comparison, the F814W data from the HDF-N (Williams et al. 1996) are also plotted. The agreement is good, with the F160W

plot possibly having a slightly steeper slope, opposite of what was observed in the HDF-N (Thompson 2003).

We are extremely grateful to Massimo Stiavelli, Bahram Mobasher, and Louis Bergeron for pointing out objects in our reduction that did not appear in their independent reduction of the same data and for providing one of us (R. I. T.) with the images for detailed comparison. We are grateful to all the personnel at the Space Telescope Science Institute (STScI), in particular Beth Perriello, who worked very hard to make the NICMOS UDF observations a success. This task was made even more difficult by the NCS safing that delayed the beginning of the observations. This article is based on data from observations with the NASA/ESA *Hubble Space Telescope*, obtained at STScI, which is operated by the Association of Universities for Research in Astronomy, Inc., under NASA contract NAS 5-26555. The individual researchers are funded in part by NASA grant HST-GO-09803.01-A-G from STScI. S. T. received support from the Danish Natural Research Council.

REFERENCES

Bertin, E., & Arnouts, S. 1996, A&AS, 117, 393
Bouwens, R. J., et al. 2004, ApJ, 616, L79
Fruchter, A. S., & Hook, R. N. 2002, PASP, 114, 144
Krist, J., & Hook, R. 2004, Tiny Tim User's Guide, version 6.2 (Baltimore: STScI)
Labbé, I., et al. 2003, AJ, 125, 1107
Lytle, D., Stobie, E., Ferro, A., & Barg, I. 1999, in ASP Conf. Ser. 172, Astronomical Data Analysis Software and Systems VIII, ed. D. Mehringer, R. Plante, & D. Roberts (San Francisco: ASP), 445
Mobasher, B., et al. 2004, *HST* Data Handbook for NICMOS, version 6.0 (Baltimore: STScI), chaps. 4.1.2 and 4.1.3, http://www.stsci.edu/hst/nicmos/documents/handbooks/DataHandbookv6
Thompson, R. I. 2003, ApJ, 596, 748
Thompson, R. I., Storrie-Lombardi, L. J., Weymann, R. J., Rieke, M. J., Schneider, G., Stobie, E., & Lytle, D. 1999, AJ, 117, 17
Thompson, R. I., Weymann, R. J., & Storrie-Lombardi, L. J. 2001, ApJ, 546, 694
Williams, R. E., et al. 1996, AJ, 112, 1335